NUMERICAL MODELING IN TIMBER ENGINEERING – MOISTURE TRANSPORT AND QUASI-BRITTLE FAILURE

Josef Eberhardsteiner, Sebastian Pech, Maximilian Autengruber, Christoffer Vida, Markus Lukacevic, Markus Königsberger, Josef Füssl

Summary

With the rising popularity of timber structures and the increasing complexity of timber engineering projects, the need for numerical simulation tools specific to this building material is gaining rapidly in importance. In particular, moisture transport processes and the quasi-brittle failure behavior, both difficult to describe, present major challenges and are of great relevance in practical construction. For these reasons, this article presents numerical modeling concepts for predicting moisture gradients, estimating effective stiffness and strength, and numerically identifying potential cracking mechanisms in wooden components. These concepts are validated through experimental test programs, and the associated challenges are addressed. Selected results ultimately demonstrate the capabilities and relevance of such methods for timber engineering.

Keywords: wood; moisture transport modeling; quasi-brittle failure; GLT; size effect; phase-field approach.

1. INTRODUCTION

Timber engineering has seen a substantial boom in recent years due to several factors. These include (i) a growing emphasis on ecology and sustainability within the building sector, (ii) a significant improvement in the quality and availability of innovative wood products, and (iii) the ability to reliably incorporate these wood products into complex engineering structures or multi-storey constructions. However, the extensive variability of building elements (both reinforced and non-reinforced), fasteners, and other special connections or built-in parts, presents challenges in evaluating and modeling the mechanical performance of wooden structures. Mechanical properties are almost exclusively determined through experimentation, a process that requires considerable

effort. Consequently, mechanical information is often generated only for select elements, specific load situations, and to a limited extent. This approach proves unsatisfactory for both the design of complex engineering structures and the advancement of technical guidelines and standards.

One approach to address this issue is to augment experimental test programs with numerical simulations, which offer several advantages: (i) They can provide a wealth of mechanical information about the component under examination. For instance, states of deformation, strain, and stress can be determined at any point of a structural element under investigation, without the limitations imposed by certain measurement methods found in experiments. (ii) Given a validated numerical model, a wide range of variants can be analyzed, and comprehensive parameter studies can be conducted. This approach facilitates the generation of a satisfactory database for a specific problem, enabling meaningful development of guidelines and standards. (iii) Particularly for larger components, like deep glulam beams or cross-laminated timber elements, the costs of numerical simulations are substantially lower than those associated with equivalent experimental testing programs.

However, to leverage these advantages, numerical models that can realistically predict the mechanical behavior of complex timber components are needed. Several challenges need to be considered: (i) Reliable material parameters must be available as input for numerical simulations, (ii) the variability of the naturally grown material wood, for example, due to knots and knot groups, as well as the pronounced orthotropic material behavior, may need to be modeled, (iii) material non-linearities, such as quasi-brittle failure mechanisms, need to be considered for certain problems. (iv) Lastly, the validation of a simulation tool based on select experiments is essential to assess the quality of the prediction and enhance the reliability of the simulation results. While scientific activity in this area is on the rise, a general simulation tool capable of addressing all the above points for arbitrary issues in timber engineering is still not available.

In this article, we aim at highlighting the potential that future numerical simulation tools will offer. For this purpose, we have selected two topics of increasing relevance in timber engineering: (i) the numerical modeling of moisture transport processes in wood, and (ii) the modeling of quasi-brittle failure mechanisms in wooden components. In this article, we present a condensed form of our recently developed methods for both subject areas, and discuss the main results.

Chapter 2 reviews the current status of moisture modeling in wood (Section 2.1) and introduces a model capable of describing moisture transport processes below and above the fiber saturation point of wood (Section 2.2). A consistent set of input parameters for

these calculations is provided, along with selected validation examples (Section 2.3). Building on these results, Section 2.4 proposes an engineering approach for determining moisture gradients in wood cross-sections relative to the ambient humidity.

Chapter 3 presents an approach to predict the bending strength of glued laminated timber (GLT) beams (Section 3.1), and demonstrates how numerical simulation analyses can contribute to the ongoing debate about the significant 'size effect' (Section 3.2). Hundreds of simulations performed on beams up to 3.3m in depth illustrate the potential and capabilities of modern simulation tools. However, knot groups and other defects in wooden boards are not considered in detail, but are represented by section-wise effective parameters, which are challenging to determine.

Chapter 4 introduces an approach, the phase-field method (Section 4.1), which can stably describe complex failure mechanisms in orthotropic materials, thereby offering a way to generate reliable effective properties for wood in the future. The potential of this method to describe wood is discussed in Section 4.2. The contribution is concluded in Chapter 5.

2. THE MODELING OF MOISTURE TRANSPORT IN WOOD PRODUCTS

Wood, a natural building material, interacts with the surrounding climate due to its hygroscopic cell walls. Besides the impact of wood moisture on the material properties (density, stiffness, strength, temperature, and moisture transport properties) [1], it also affects the cross-sectional dimensions. The direction-dependent expansion coefficients β can induce residual stresses, which may, alone or in conjunction with existing stresses, lead to cracking. Furthermore, wood moisture contributes to long-term deformations via mechano-sorptive and viscoelastic creep.

Water can be found in wood in three interrelated forms: (i) bound water in the cell walls, (ii) water vapor in the cell lumen, and (iii) free water in the cell lumen. Transport within these phases can be described through diffusion (bound water and water vapor) or capillary transport (free water). Wood moisture is defined as the mass of water in relation to the mass of oven-dried wood ρ_d [3], disregarding the mass of water vapor.

In the drying process that commences after the tree is felled, free water in the cell lumen is first reduced, while the cell wall and the water vapor pressure (owing to the small volume) can be assumed to remain saturated. During this phase, the pits, which act like valves between cells during drying, may not always completely close [4]. At the so-called fiber saturation point (FSP), the free water has evaporated, but the cell wall remains fully saturated.

If the drying process continues, the moisture in the cell wall and the water vapor pressure in the lumen decrease until an oven-dry state is attained. The theoretical concept of the FSP [5] differs from practice, where transitions are continuous, leading to the notion of a fiber saturation area rather than a distinct point [6].

The area below the FSP is of primary interest for stress determination, as changes in wood properties and shape are tied to changes in cell wall moisture (hygroscopic area).

2.1. State of the Art

Determining the moisture state in a wooden component, which varies both spatially and over time, is complex. Consequently, the current version of the standard for the design and construction of timber structures [7] (EC 5) offers a simplified approach to consider moisture in wood, based on three empirically derived parameters.

In the ultimate limit state design methodology, one of three service classes (NKL) must be selected based on the prevailing relative humidity, temperature, wood moisture content, and the type of structure or building. The NKL, coupled with load duration, defines a reduction factor k_{mod} for the material strength. Other influences, like cross-sectional dimensions, are not accounted for. For managing cracks in cases of shear, factor k_{cr} reduces the cross-section width by a certain amount. As noted in [8], changes in stiffness and residual stresses due to moisture variations in EC 5 are currently not directly considered in the ultimate limit state design concepts. The wood moisture content is incorporated in the serviceability limit state through the parameter k_{def}, which influences material stiffness and is designed to account for creep deformations.

In scientific literature, a rough distinction is drawn between (i) the simple Fickian model for describing moisture transport in the hygroscopic range, where moisture transport is represented by a Fickian diffusion equation (combining the moisture content in the cell wall and lumen into an effective value, with equilibrium always existing between the two phases), and (ii) the multi-Fickian model described by two coupled Fickian diffusion equations (with separate moisture content in cell walls and lumen and no equilibrium between the phases).

While the simple model yields sufficiently accurate results in cases of low relative humidity and thin material, the more complex model is preferable in other scenarios [9]. In [2], the multi-Fickian model is merged with the transport of free water above the FSP. This leads to a unified model capable of describing all phases of water in wood independently. This model is presented in the following section.

2.2. Finite-element-based simulation concept

The presented moisture and temperature transport model utilizes volume-averaged transport equations. This approach defines a representative volume element (RVE) at the macroscopic level of wood (encompassing several cells), which allows all occurring phases to be described as a continuum [10].
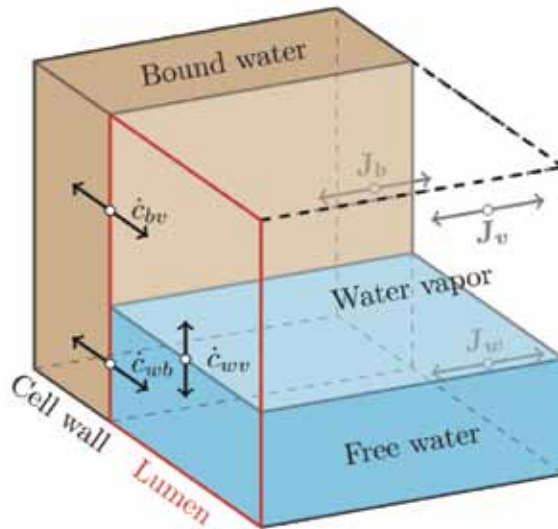
Figure 1.States of water in a representative volume element (RVE). Bound water in the cell wall (brown), water vapor and free water in the lumen. Exchange between the phases occurs by sorption ($\dot{c}_{wb}$ from free to bound water and from $\dot{c}_{bv}$ bound water to water vapor) and evaporation/condensation $\dot{c}_{wv}$ between free watebvand water vapor. The transport within each phase is denoted by J_w for free water, J_b for bound water, and J_v for water vapor. [2]
Slika 1. Stanje vode u reprezentativnom volumnom elementu (RVE). Rubna voda u stjenki ćelije (smeđe), vodena para i slobodna voda u šupljini. Fazna razmjena javlja se sorpcijom ($\dot{c}_{wb}$ iz slobodne u rubnu vodu i $\dot{c}_{bv}$ iz rubne vode u vodenu paru) i isparavanjem/kondenzacijom $\dot{c}_{wv}$ između slobodne vode i vodene pare. Prijenos unutar svake faze je označen s J_w za slobodnu vodu, J_b za rubnu vodu i J_v za vodenu paru [2].

The three variables required to describe the phases of water are defined relative to the volumes depicted in Figure 1: the concentration of free water c_w across the entire RVE, the concentration of bound water c_b over the entire RVE, and the concentration of water vapor c_v in the gas-filled portion of the lumen (which includes both water vapor and dry air). The phase transition terms account for the lumen's saturation S_w. $\dot{c}_{wb}$ is defined in the portion of the volume containing free water, while $\dot{c}_{bv}$ acts in the rest of the lumen.

With the assumptions made in [2] and the considerations on the transport mechanisms based on the RVE from Figure 1, the subsequent balance equations can be established:

Conservation of bound water concentration c_b:

$$\frac{\partial c_b}{\partial t} = -\frac{\partial}{\partial x} \cdot \mathbf{J_b} + \dot{c}_{bv} + \dot{c}_{wb} \tag{1}$$

Conservation of water vapor concentration c_v:

$$\frac{\partial c_v f_{lumgas}}{\partial t} = -\frac{\partial}{\partial x} \cdot \mathbf{J_v} f_{lumgas} - \dot{c}_{bv} + \dot{c}_{wv} \tag{2}$$

Conservation of free water concentration c_w:

$$\frac{\partial c_w}{\partial t} = -\frac{\partial}{\partial x} \cdot \mathbf{J_w} - \dot{c}_{wb} - \dot{c}_{wv} \tag{3}$$

Conservation of energy:

$$\frac{\partial \rho h}{\partial t} = -\frac{\partial}{\partial x} \cdot \mathbf{f} - \frac{\partial}{\partial x} \cdot \mathbf{J_b} \bar{h}_b - \frac{\partial}{\partial x} \cdot \mathbf{J_v} h_v f_{lumgas} - \frac{\partial}{\partial x} \cdot \mathbf{J_w} h_w \\ + \dot{c}_{bv}(h_v - h_b) + \dot{c}_{wb}(h_w - h_b) + \dot{c}_{wv}(h_w - h_v) \tag{4}$$

On the left side of the equations (1)–(4), there are the temporal changes in the respective variable, and on the right side, the spatial changes in the current fluxes $\mathbf{J}$ together with the phase transition terms (sorption rates $\dot{c}_{wb}$ and $\dot{c}_{bv}$ as well as evaporation/condensation rate $\dot{c}_{wv}$). In energy conservation, the heat flow density $\mathbf{f}$ also occurs. The definitions of the phase transitions are described in detail in [2].

The equation system is numerically solved utilizing the Abaqus software via a user element subroutine. Spatial discretization is accomplished through the finite element method, while time integration is conducted using the implicit Euler method. The equation system is resolved employing the modified Newton method.

The multi-Fickian moisture transport model beneath the FSP has been extensively studied and validated in other literature [11, 12, 13]. Therefore, the focus in [2] centers on examples that encompass free water to investigate both this aspect and the transition between conditions beneath and above the FSP. For model validation, experiments and simulations from literature are presented in the subsequent section. The values of the material parameters and the defining equations can be found in [2].

2.3. Model validation

A total of seven different validation examples are considered (see Table 1).

Table 1. Comparison of the seven validation examples examined. Red markings indicate drying processes and blue markings indicate wetting/infiltration processes. The type "E" denotes experiment and "S" simulation. The length of the specimen is indicated in the direction of the one-dimensional transport process.

Tablica 1. Usporedba sedam ispitanih validacijskih primjera. Crveno označavanje pokazuje proces sušenja i plavo označavanje pokazuje proces vlaženja/infiltriranja. Tip „E" označuje eksperiment a „S" simulaciju. Duljina uzorka je uzeta u pravcu jednodimenzijskog prijenosnog procesa.

#	Type	Direction/ Length	Initial Conditions			Boundary Conditions			Source
			T [°C]	RH [%]	MC [%]	T [°C]	RH [%]	MC [%]	
①	S	T/16,2 mm	20	54	8.16	20	75	-	(Konopka & Kaliske, 2018)
②	S	R/20 mm	25	100	100	50	32	-	(Perré, 2015)
③	E,S	R/31 mm	50	100	135	50	43	-	(Eriksson, Johansson, & Danvind, 2007)
④	E	R/25 mm	25	100	90	50	25	-	(Sandoval-Torres, Pérez-Santiago, & Hernández-Bautista, 2019)
⑤	E	T/9 mm	22	100	160	22	40	-	(Gezici-Koç, Erich, Huinink, van der Ven, & Adan, 2017)
⑥	E	T/9 mm	22	33	5.3	22	100	160	(Gezici-Koç, Erich, Huinink, van der Ven, & Adan, 2017)
⑦	E	L/350 mm	23	62	11	23	100	100	(Krabbenhøft & Damkilde, 2004)

In Example ①, the model presented is compared with simulations below the FSP from [10] and [9], with excellent alignment observed. Example ② examines the drying process starting from green wood. The results from the proposed model are compared with simulations from [14]. Besides showing a very good match across the entire simulation, the characteristic wet-bulb temperature of drying experiments is also evident. Good agreement is also found in the drying simulation from [15], which is examined in Example ③. Furthermore, a variant in which the exponent of the relative permeability is reduced from 3 to 2 is analyzed. As shown in Example ④, when modeling the drying experiment from [16], this adjustment led to a slightly better agreement with the test results.

Contrasting with the previous experiments, the study in [17] involved re-moistening previously dried wood, followed by a second drying process. Therefore, in Example ⑤, the experimental results cannot be exactly replicated using the existing material characteristics. This discrepancy might be explained by the opening and closing behavior of the wood pits when re-moistened and dried.

In addition, two examples of infiltration are examined (Example ⑥, extracted from [17], focuses on infiltration in the radial direction, and Example ⑦, taken from [4], explores infiltration in the longitudinal direction). The material parameters are adjusted for these two cases, and the transfer coefficient for free water, for which no literature sources are known, is calibrated. This enables a more accurate simulation of the infiltration behavior.

In the following sections, the validation examples ② and ⑦ are presented in more detail:

2.3.1. ② *Simulation Perré (Perré, 2015):*

In [14], a drying process based on a wood moisture content of 100 % was simulated over 50 hours. The drying took place exclusively in the radial direction along the 20 mm long specimen with a dry bulk density of 500 kg m^{-3}.

During the simulation, the temperature is increased from the initial 25 °C to 50 °C, and the relative humidity of the environment is set at 32 %. The transfer coefficients are given as 14 W m^{-2} K^{-1} for the heat transfer k_T, and 0,014 m s^{-1} for the mass transfer k_{cv}. The parameters for describing the sorption isotherm are adapted to the definition from [18] at the temperature of 50 °C.

Figure 2. The curve of moisture content and temperature during 50 h drying in radial direction. Shown are the present model – as well as the models from [14] with constant ("Model 1" in red) and variable transport coefficients ("Model 2" in blue). The exchange with the environment takes place exclusively through the red marked area at the left end. [2]

Slika 2. Krivulja sadržaja vlage i temperature za vrijeme od 50 sati sušenja u radijalnom smjeru. Prikazani su sadašnji model kao i modeli iz [14] s konstantnim („Model 1" crveni) i promjenjivim prijenosnim koeficijentima („Model 2" plavi). Razmjena s okolinom nastaje na lijevom kraju preko područja koje je označeno crvenom bojom
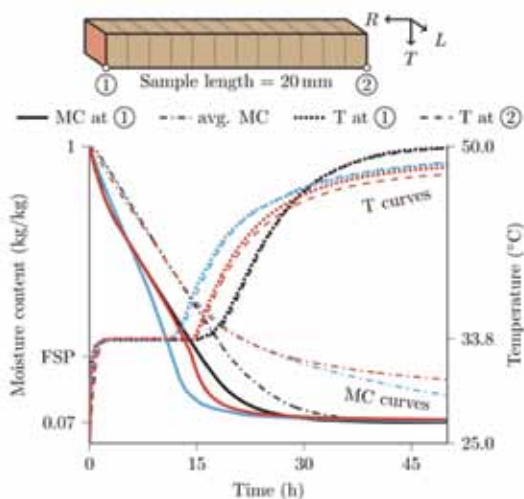
[2].

As Figure 2 shows, the model can accurately depict the drying process, as well as the model from [14]. In the initial phase, the temperature rises from the initial 25 °C to the wet-bulb temperature of approximately 33.8 °C. As soon as the moisture level at point j on the boundary falls below the FSP, the temperature begins to rise towards the boundary condition level, contingent upon the evaporation rate of free water. The differences between the two simulations presented in literature result from the different treatment of the transport terms, which are either constant ("Model 1") or simplified and dependent on the wood moisture content ("Model 2").

2.3.2.⑦ *Experiment Krabbenhøft und Damkilde (Krabbenhøft & Damkilde, 2004):*

The infiltration of the 350 mm long test body made of fir wood is described in [4] in two phases, first a fast infiltration in the form of the α-phase in the large lumen, then in small cavities by means of the β-phase. The transport coefficient of the α-phase determined in [4] is used for the transport of free water. The transfer coefficient for free water k_{cw} is assumed to be 1.3 E-5 m s^{-1}, and the heat transfer coefficient k_T to be 25 W m^{-2} K^{-1}. No boundary condition is applied for water vapor, since this value is influenced by the evaporation of free water.

Figure 3. The moisture content profiles of a one-dimensional infiltration process shown longitudinally after 6 d, 8 d, 15 d, and 21 d along the path from j to k. The initial moisture content is 11 % at RH = 62 % and 23 °C. The boundary conditions equivalent to a moisture content of 100 % at the temperature of 23 °C are applied to the side surface marked in blue. [2]

Slika 3. Profili sadržaja vlage za jednodimenzijski proces infiltracije prikazan uzdužno poslije 6d, 8d, 15d i 21d duž puta od (1) do (2). Početni sadržaj vlage je 11% za RH = 62% i 23 °C. Rubni uvjeti ekvivalentni sadržaju vlage od 100 % kod temperature od 23 °C primjenjuju se na površini koja je označena plavom bojom [2].
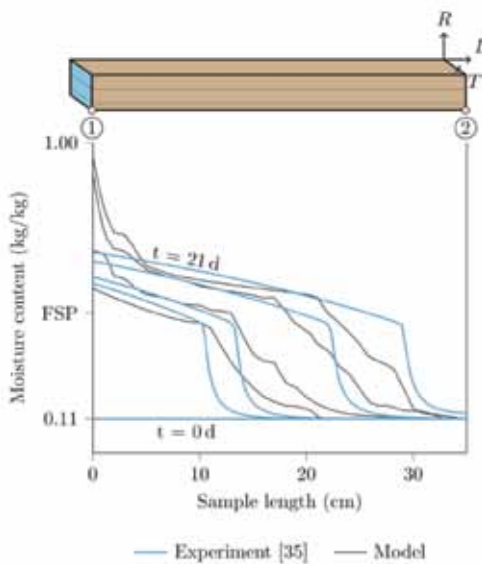
Figure 3 displays the wood moisture profiles after 6, 8, 15, and 21 days of infiltration. A kink can be discerned in the profiles around 45 % wood moisture, attributable

to the shift in the transport mechanisms at the FSP. By adjusting the FSP from approximately 30 % wood moisture to the plateau level of around 45 %, the experimental results could be very closely replicated. However, the β-phase is not included in the presented model, meaning that these effects cannot be accounted for. Aside from this, the model accurately represents the distribution of wood moisture and the evolution of the profiles, characterized by a rapid frontal propagation through the mechanisms below the FSP, followed by an increase through the mechanisms above the FSP.

2.4. Prediction concept for moisture-induced stresses solely using relative humidity data

With the validated model, we can now address practical problems. As mentioned at the beginning, the distribution of wood moisture in a cross-section is currently only indirectly considered in the verification process via the scaling of material parameters. To attain a more precise evaluation, in [19], various cross-sections of solid and glued laminated timber (GLT) are initially exposed to the climate of Linz, Austria, for a period of 14 months. The resulting wood moisture distributions are then determined, as illustrated in Figure 4 for the GLT 20/40 cross-section. As for the environmental conditions, it is assumed that the cross-sections under consideration are exposed to the outdoor climate but shielded from direct water ingress, such as rain.
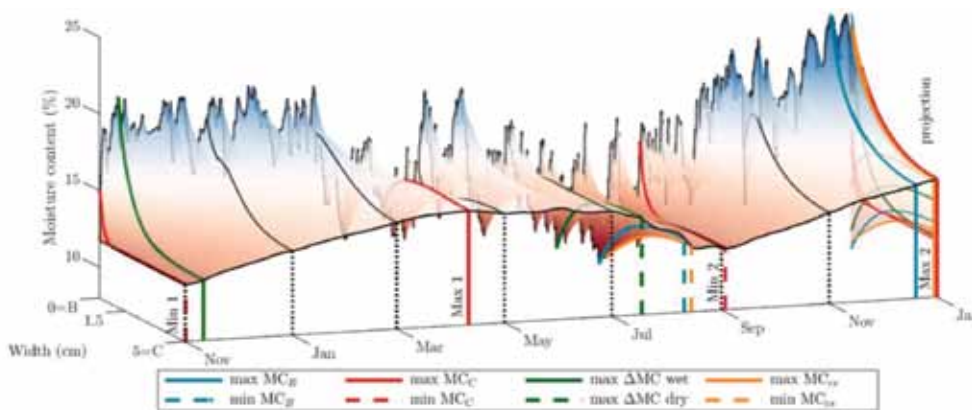
Figure 4. The course of moisture content along the horizontal axis of symmetry of a GLT 20/40 from B to C in the period from November 1, 2014 to December 31, 2015. Marked are the points in time at which maximum and minimum moisture contents occur in B and C, as well as the largest differences in moisture content between B and C.
Slika 4. Tijek sadržaja vlage duž horizontalne osi simetrije za GLT 20/40 od B do C u periodu od 1. studenoga 2014. do 31. prosinca 2015. Tim točkama označeno je vrijeme za koje se maksimalni i minimalni sadržaji vlage javljaju u B i C, kao i najveća razlika u sadržaju vlage između B i C.

From Figure 4, it can be observed that the points near the edge respond rapidly to changes in the ambient relative humidity, whereas the points near the center exhibit a significantly slower response to these changes. Based on the envelope curves, which are derived from the maximum and minimum wood moisture levels along the path from B to C (as seen on the right in Figure 4), an exponential function is employed for wide cross-sections like the GLT 20/40 in [19]:

$$MC(x) = MC_C + F \exp(x^a) \tag{7}$$

The parameter MC_c indicates the wood moisture content at point C, which can be determined by utilizing the average relative air moisture content throughout the entire period under consideration and the adsorption isotherm. For the GLT 20/40 cross-section, a value of 0.8 has been found to be the most suitable for parameter a. The parameter F varies for the horizontal and vertical paths, as well as for the drying and humidification cases.
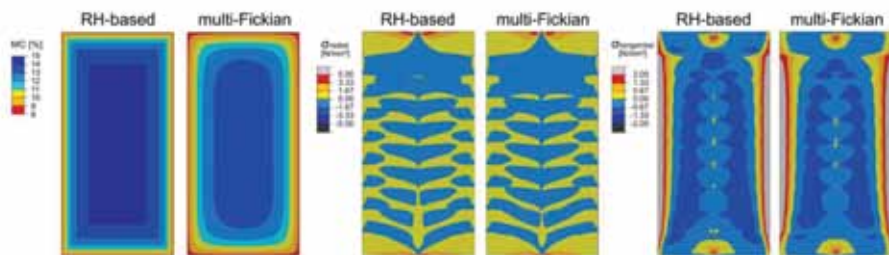
a) Case drying – moisture content, radial and tangential normal stresses.
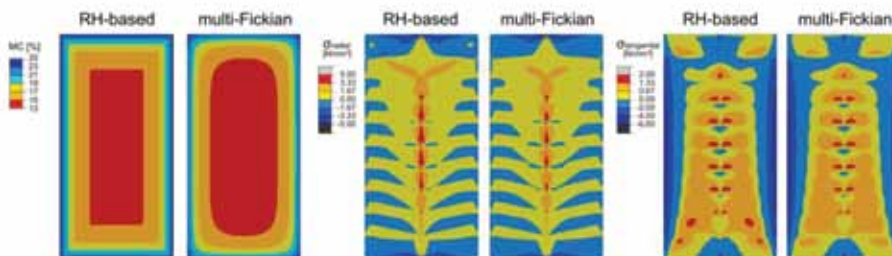
b) Case wetting – moisture content, radial and tangential normal stresses.

Figure 5. A comparison of moisture contents and radial and tangential stresses of the simplified model based purely on relative humidity (left graphs), and the multi-Fickian transport model (right graphs) during drying (a) and wetting (b) of cross-section GLT 20/40. The gray areas exceed the tensile strengths of about 5 MPa in radial and about 2 MPa in tangential direction, respectively [19].

Slika 5. Usporedba sadržaja vlage i radijalnih i tangencijalnih naprezanja pojednostavljenog modela koji se temelji isključivo na relativnoj vlažnosti (lijevi crteži) i multi-Fickianski transportni model (desni crtež) za vrijeme sušenja (a) i vlaženja (b) presjeka za GLT 20/40. U sivom području vlačna čvrstoća premašuje oko 5 MPa u radijalnom i oko 2 MPa u tangencijalnom smjeru [19].

In the subsequent step, both paths are evaluated for each point of the two-dimensional cross-section and combined using a minimum function for drying or a maximum function for wetting. This results in a two-dimensional wood moisture distribution solely based on the relative humidity, as depicted on the far left in Figure 5. With this information, along with a stiffness tensor and moisture expansion coefficient β from a source such as [20], the stress distribution caused by wood moisture in the cross-section can now be determined (Figure 5, middle and right).

The resulting wood moisture field is compared with that of the multi-Fickian transport model at critical time points from [20]. It is evident that the wood moisture levels exhibit excellent agreement, although the field deviates slightly more towards the corners due to the use of the minimum/maximum function. The resulting normal stresses in the R and T directions also demonstrate a strong agreement (Figure 5).

As mentioned in the introduction, in addition to describing moisture transport in wood, predicting failure mechanisms and collapse loads presents a significant challenge. Consequently, the focus of the following two chapters centers on this topic.

3. THE PREDICTION OF THE BENDING STRENGTH OF GLUED LAMINATED TIMBER BEAMS

3.1. Finite element-based simulation concept

According to [23], the bending strength of a GLT beam is dependent on the tensile strengths of the assembled lamellas. The local inhomogeneity in the wood structure plays a crucial role in determining a lamella's tensile strength and longitudinal stiffness. Using four-point bending tests [24] (see Figure 6), additional evidence for the influence of beam depth on derived bending strengths has been presented, as exemplified in [25], where the strengths were observed to decrease with an increase in depth. This size effect can be attributed to the increasing probability of a defect as beam dimensions increase, as per the Weibull theory [26]. However, according to [27], it can also be explained by a quasi-brittle failure of weak points in the wood structure, consistent with non-linear fracture mechanics. Therefore, giving adequate consideration to inhomogeneity and chosen failure mechanisms is crucial for estimating the global failure of a GLT beam. Another vulnerability lies in the connection of two boards through finger joints. [28] demonstrated that the tensile strength of a finger joint could be modeled equivalently to that of an imaginary branch of a specified size.
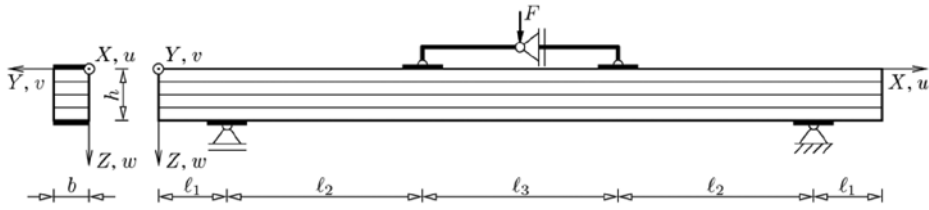
Figure 6. The four-point bending test in accordance with [24] with the total load *F* and the dimensions for depth *h*, width *b*, and lengths l_i.

Slika 6. Test savijanja s četiri točke u skladu s [24] s ukupnim opterećenjem *F* i dimenzijama za dubinu *h*, širinu *b* i duljinu l_i.

The three-dimensional computational modeling approach presented in this study is based on the method proposed in [29]. It simulates sections of a GLT beam in a four-point bending test to estimate bending strengths. The beam sections are composed of individual boards. Each board comprises defect-free sections, sections with individual knots, or groups of knots. The corresponding material properties are directly based on the morphology of actual boards, with data acquisition taking place during machine strength grading. For each board, a stiffness tensor was determined, analogous to [30], and a longitudinal stiffness and tensile strength profile were derived, in accordance with [31]. This process results in the virtual description of 140 boards, each belonging to strength classes T14 and T22. These descriptions include an accurate distribution of weak points and constant properties with respect to sections. The boards measure 5400 mm in length, 90 mm in width, and 33 mm in thickness.

The simulated beam section lies within the region where a constant bending moment exists during the test. At both ends of this section, load introduction sections with lengths of 100 mm are added (refer to Figure 6). Therefore, each simulation represents only the governing section where the beam is likely to fail. Load introduction and support are defined by specifying boundary conditions at the reference points R_1 and R_2 (see Figure 7). The homogeneous boundary conditions specify the bearing, and are as follows:

$$R_1: \varphi_X^{R_1} = \varphi_Z^{R_1} = 0, u^{R_1} = w^{R_1} = 0, \tag{8a}$$

$$R_2: \varphi_X^{\bar{R}_2} = \varphi_Z^{\bar{R}_2} = 0. \tag{8b}$$

The load is applied through inhomogeneous boundary conditions, with opposing imposed rotations ϕ about the Y-axis generating a constant moment along the beam section:

$$R_1: \varphi_Y^{R_1} = -\phi, \tag{9a}$$

$$R_2: \varphi_Y^{R_2} = \phi. \tag{9b}$$

Additionally, the existing symmetry is leveraged by inhibiting displacements in the Y-direction within the symmetry plane.
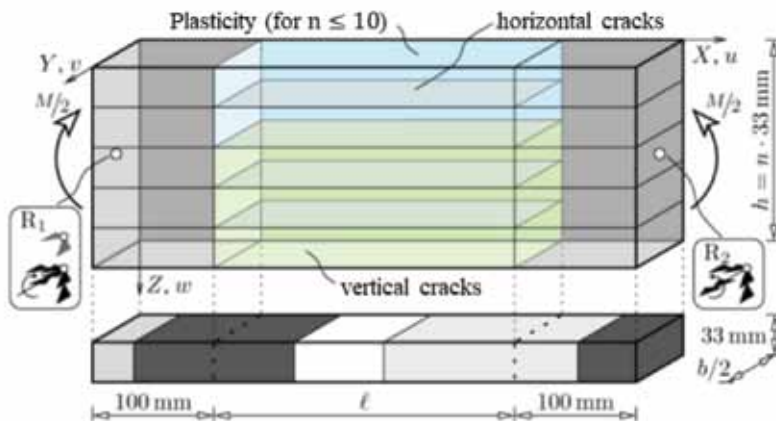
Figure 7. The modeling approach forms a beam section of length *l* and load application lengths of 100 mm from single boards with section-wise constant material properties (shading) with boundary conditions, applied load *M/2*, consideration of symmetry properties, the realization of vertical and horizontal cracks (green region), and for $n \leq 10$ with implementation of plastic material behavior (blue region).

Slika 7. Postupak modeliranja odnosi se na presjek grede duljine *l* i opterećenje po duljini od 100 mm pojedinačnih ploča s konstantnim svojstvima materijala po presjecima (osjenčano) s rubnim uvjetima, narinuto opterećenje *M*/2 , razmatranim svojstvima simetrije, uzimanjem u obzir vertikalnih i horizontalnih pukotina (zelena regija), a za $n \leq 10$ s implementacijom plastičnog ponašanja materijala (plava regija).

The simulation is implemented in the Abaqus 2021 software using a non-linear finite element method. The discretization is performed with hexahedral elements and trilinear shape functions (24 degrees of freedom). The element size is approximately 16.5 mm in the X-direction, with two elements allocated over the height of a lamella and three over the width. A mesh size study revealed that the chosen element size is sufficiently small. The material model for the boards is orthotropic and generally linearly elastic. However, local plasticizing under compression leads to a decrease in load-bearing capacities, which is particularly non-negligible for smaller beam sizes and higher strength classes [25]. Therefore, for beams composed of up to 10 lamellas, the multi-surface plasticity model [32, 33, 34] is applied on the compression side (see the blue region in Figure 7).

The quasi-brittle beam failure is simulated via purely vertical cracks within a lamella and horizontal cracks between lamellas (see the green region in Figure 7). This allows for continuous cracks across multiple laminations, such as when two vertically spaced cracks in adjacent

laminations are connected by a horizontal crack. Global failure, and thus the load-bearing moment of a beam, is defined by at least a 3 % decrease in the acting moment from the previous maximum moment. The two crack orientations are described in more detail as follows:

- Vertical cracks are implemented using the extended finite element method and a traction-separation law. This method allows the splitting of a finite element by a crack. Crack initiation or growth occurs after the specified tensile strength of the material is exceeded. The applied law defines crack development. The traction stress between the crack surfaces is defined by the distance between them and the given fracture energy G_f. For all sections, the fracture energy is assumed constant as $G_f = 30$ N mm/mm^2. In a fully developed crack, there is no interaction between the two crack surfaces. In addition, the approach uses crack stabilization with a viscosity coefficient of $1 \cdot 10^{-6}$.

- Horizontal cracks are achieved using a cohesive contact condition in conjunction with a traction-separation law. The contact condition defines the connection between the lamellas by prescribing the stiffness in the normal direction, as well as both shear directions, which are set constant at 10,000 N/mm^2. When either of the assumed strengths $f_n = 5$ N/mm^2 or $f_p = f_q = 5$ N/mm^2 is reached, the law manages the decrease of the traction stresses, similar to the process for vertical cracks. In this case, the fracture energy maintains a constant value of $G_f = 0.6$ N mm/mm^2, and the stabilization uses a viscosity coefficient of $1 \cdot 10^{-5}$.

For validation, the bending strengths of 40 homogeneously assembled beams from an experimental study [25] were simulated and compared with the experimental results. The simulations replicate the real beam structure using the previously described virtualized boards. Exact replication is possible because the real beams were constructed from these boards. For this purpose, the length l of the simulated beam sections (refer to Figure 7) corresponded to the length l_3 from the experiments (see Figure 6). Overall, the validation incorporated two strength classes and two beam sizes, divided into four types with ten beams each (refer to Table 2, with strength values as defined in the EC5).

Table 2. The specification of the tested types of beams with the characteristic tensile strength of a lamella in the longitudinal direction $f_{t,0,k}$, as well as the characteristic bending strength of the beam $f_{m,k}$ (strengths according to [23]), the number of lamellas n and its dimensions according to Figure 6. All beams had a width $b = 90$ mm.
Tablica 2. Specifikacija ispitanih tipova greda s karakterističnom vlačnom čvrstoćom lamele u uzdužnom smjeru $f_{t,0,k}$ kao i čvrstoćom savijanja grede $f_{m,k}$ (čvrtoća prema [23]), broj lamela n i njihove dimenzije prema slici 6. Sve grede su imale širinu $b = 90$ mm.

	Lamellas		GLT beam			Dimensions				
Type	Strength class	$f_{t,0,k}$ [N/mm²]	Strength class	$f_{m,k}$ [N/mm²]	n	$2l_2 + l_3$ [mm]	l_1 [mm]	l_2 [mm]	l_3 [mm]	h [mm]
A	T14	14.0	GL 24h	24.0	4	2340	180	780	780	132
B	T22	22.0	GL 30h	30.0						
D	T14	14.0	GL 24h	24.0	10	5200	100	1610	1980	330
E	T22	22.0	GL 30h	30.0						

According to [24], the bending strength f_b is calculated from the ultimate load F_{max} and the cross-section dimensions with width b and depth h as follows:

$$f_b = \frac{3\,l_2 F_{max}}{b h^2},$$ (10)

where l_2 describes the horizontal distance between the support and the nearest load application (see Figure 6). In the simulations, the ultimate load is calculated from the ultimate moment M_{max} according to:

$$F_{max} = \frac{2\,M_{max}}{l_2}.$$ (11)

The validation process yields a coefficient of determination of 0.62 for the bending strength of the considered beams. The mean values derived from the ratios of simulated to experimental bending strengths are 1.02 for type A, 0.97 for type B, 1.05 for type D, and 0.92 for type E.

3.2. The investigation of the size effect for the GLT beams

The size effect was further investigated using homogeneous beam sections with a random assembly. Hence, the virtualized boards of two strength classes, T14 and T22, were assembled into beams of classes GL 24h and GL 30h. Beams with an l/h ratio of 1.5 and the following beam depths h were investigated in the study: 165 mm, 330 mm, 660 mm, 1320 mm, 1980 mm, and 3300 mm. This corresponds to beams with 5, 10, 20, 40, 60, and 100 laminations, with 500, 100, 100, 100, 100, and 50 simulations per strength class, respectively. The randomized design of each section was based on the following steps:

- random selection of each lamella from the entire collection of boards,
- random starting position of the lamella within the selected board, allowing only starting positions, with which the lamella can cover the length of the beam section,
- random definition of the direction of the lamella's course.
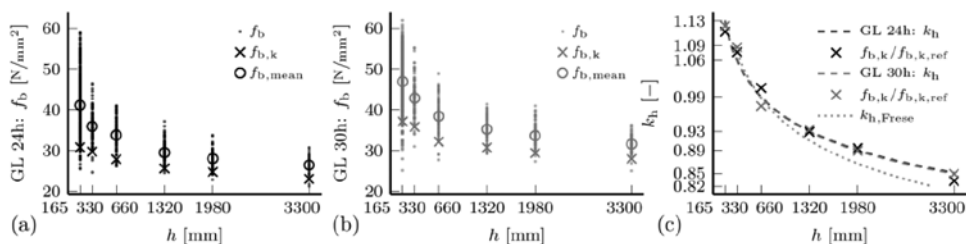
Figure 8. An illustration of the size effect using (a,b) the bending strengths f_b of both strength classes, with the characteristic strength $f_{b,k}$ and the mean strength $f_{b,mean}$ from log-normal distributions, and (c) the functions of the coefficients k_h with the corresponding reference strengths $f_{b,k,ref}$ of each strength class, and comparison to $k_{h, Frese}$ according to [35].

Slika 8. Prikaz učinka veličine korištenjem (a,b) čvrstoće savijanja f_b za karakterističnu čvrstoću $f_{b,k}$ i srednju čvrstoću $f_{b,srednje}$ iz logaritamskih normalnih raspodjela i (c) funkcije koeficijenata k_h s odgovarajućim referentnim čvrstoćama $f_{b,k,ref}$ za svaki oblik čvrstoće i usporedba s $k_{h, Frese}$ prema [35].

The estimated bending strengths f_b are shown in Figure 8a,b for one strength class at a time. The characteristic strength $f_{b,k}$ and the mean value of the strength $f_{b,mean}$ at each beam size (see Figure 8a,b) were determined from the log-normal distributions estimated by the maximum likelihood method. The size effect observed with the simulations is shown in Figure 8c over the coefficient k_h for both strength classes. Here, k_h is in the format of EC 5, and the functions shown are:

$$k_h = \left(\frac{600}{h}\right)^{1/m} \text{ with } m = \begin{cases} 10.3796 & \text{GL 24h} \\ 10.2482 & \text{GL 30h} \end{cases} \tag{12}$$

where the parameter m and the reference strengths $f_{b,k,ref}$ for $h = 600$ mm with $k_h = 1.00$ (for GL 24h: 27.66 N/mm^2 and GL 30h: 33.05 N/mm^2) were determined using the least squares method. In [28], a modeling approach was developed, which observed a decrease in the scatter of bending strengths, but no decrease in the strengths themselves for beam depths ranging from 320 mm to 1200 mm. In [35], a decrease in strengths was found, with increasing depth using the "Karlsruhe calculation model" for beam depths investigated between 300 mm and 3000 mm. A value for k_h was determined for this, and the result is shown for comparison in Figure 8c.

Even though the model and related simulation program presented here is one of the most advanced in describing the size effect of GLT beams to date, there remain some weaknesses that should be addressed in the future. The most significant uncertainty is the effective strength and fracture energy of knots and knot groups. These cannot be

meaningfully determined experimentally. To achieve this computationally, methods are required that can stably describe quasi-brittle failure mechanisms of complex structures made of an orthotropic material, like wood. A promising approach for this is the so-called phase field method, which is discussed in the following section.

4. THE PHASE FIELD METHOD-BASED MODELING OF FRACTURE IN WOOD

The fracture mechanics characteristics of naturally grown wood on the macroscopic scale depend on various phenomena, largely influenced by the microstructure. Wood is a highly orthotropic material. Crack growth begins on the microscopic scale from defects in the cell wall material. Once a macroscopic crack localizes, a fracture process zone forms [36]. Subsequently, toughening effects such as fiber bridging set in [37, 38]. The presence of microcracks and toughening effects result in cohesive material behavior. Furthermore, the microstructure significantly influences the macroscopic crack orientation. Wood fibers lie on the so-called growth surfaces with a weak interface between the fibers. This leads to cracks tending to follow the path of least resistance parallel to the fibers [36]. Spatially varying principal material directions further contribute to complex crack topologies. In summary, simulating wood fracture requires a numerical method that can account for orthotropic constitutive behavior, cohesive fracture, preferable fracture planes, and complex 3D cracks.

The phase field method for fracture is an approach that effectively accounts for the outlined features. It is rooted in Griffith's theory of brittle fracture [39], which is formulated in a variational approach [40, 41, 42, 43]. By introducing the field $d(x) \in [0,1]$, the crack discontinuity is modeled by a smooth transition zone from the uncracked state ($d(x) = 0$) to the cracked state ($d(x) = 1$). The so-called length scale parameter controls the transition zone's width, and is linked to the discretization size. This regularized form of Griffith's theory can be solved in an energy minimization scheme, and gamma-converges as the length scale parameter tends towards zero, given a sufficiently small mesh size.

In the recent years, the phase field method for fracture has been expanded to incorporate cohesive behavior, anisotropic materials, and preferable fracture planes. In [44], a multi-phase field model that allows for various failure mechanisms was proposed. Preferable fracture planes are considered in [45, 46, 47] by introducing a second-order tensor to scale the gradient of the phase field, thus invalidating specific crack propagation directions. The unified phase field theory [48] allows for the incorporation of a cohesive zones model into the formulation.

In addition to material-generic extensions of the phase field method, some research focuses specifically on phase field models for wood. In [49], microscopic-scale simulations are performed on wood, while on the macroscopic scale, [50] employs a representative crack element to model the deformation behavior of cracked regions. In [51, 52], a hybrid multi-phase field model based on the unified phase field theory is proposed and validated. The following section will focus on a more detailed discussion of this latter model.

4.1. Phase field model for wood

This work employs a multi-phase field model [44] based on the unified phase field theory [48]. The model incorporates assumptions about likely crack orientations in wood, originating from the principal material directions. Since cracks tend to propagate along these directions, but display very different fracture mechanics characteristics depending on their orientation, three separate phase fields for cracks perpendicular to the longitudinal (L), the radial (R), and the tangential (T) direction are considered. Excluding body forces and surface traction, the regularized form of the total energy of the system on the domain Ω is as follows:

$$\Pi(\mathbf{u}, \mathbf{d}) = \int_{\Omega} [\psi^+(\mathbf{u}, \mathbf{d}) + \psi^-(\mathbf{u})] \, dV + \sum_{i \in \{L,R,T\}} G_{c,i} \int_{\Omega} \gamma_i(d_i) \, dV, \tag{13}$$

where $\psi^+(u,d)$ denotes the degraded strain energy density, which defines the driving force for fracture, and $\psi^-(u)$ denotes the undegraded strain energy density. For phase field i, $G_{c,i}$ denotes the fracture energy release rate, and γ_i the so-called crack surface density function approximating a sharp crack as a diffuse volume. The crack surface density function in the unified phase field theory, including the structural tensor, is defined as

$$\gamma_i(d_i) = \frac{1}{c_{0,i}} \left(\frac{1}{l_i} \alpha_i(d_i) + l_i \nabla d_i \mathbf{A}_i \nabla d_i \right), \tag{14}$$

with $c_{0,i} = 4 \int_0^1 \sqrt{\alpha_i(\beta)} d\beta$, $\alpha_i(d_i) = 2 \, d_i - d_i^2$, as the local part of the dissipated fracture energy, and $\mathbf{A}_i = \mathbf{I} + \beta_i (\mathbf{I} - \mathbf{a}_i \otimes \mathbf{a}_i)$ as the structural tensor, where a_i is the material direction, and β_i is the scaling factor of the structural tensor for phase field i. For $\beta_i = 0$, the standard isotropic formulation for the crack surface density function is recovered.

The counterpart to energy dissipation through extending cracks is the degradation of the solid, i.e., the definition on $\psi^+(u,d)$ with respect to d. The phase field model in [51] utilizes a so-called stress-based split [53] to additively decompose the strain energy density into a crack driving and inactive part. The crack driving strain energy density for a crack perpendicular to a_i is defined based on the fracture mechanics failure modes I, II,

and III. By projecting the undamaged stress tensor σ onto a fictitious crack surface with the crack normal vector a_i, the crack driving stress σ^+ for an orthotropic material can be found [51]. Following the principle of maximum dissipation, the crack orientation i with the largest energy release, i.e., the largest $\psi_i^+(u)$, drives the crack. Thus, the strain energy terms in Equation (13) are replaced by

$$\psi_i^+(\boldsymbol{u}, \boldsymbol{d}) = \omega_i(d_i)\, \psi_i^+(\boldsymbol{u}) \quad and \quad \psi_i^-(\boldsymbol{u}, \boldsymbol{d}) = \psi_i(\boldsymbol{u}) - \psi_i^+(\boldsymbol{u}), \qquad (15)$$

where $\omega_i(d_i)$ is the degradation function of the unified phase field theory [48] for phase field i. The resulting energy minimization problem is solved using a staggered scheme [40, 54] coupled with a hybrid approach [55]. To prevent the interpenetration of cracks, a smooth traction-free crack boundary condition [56] is applied. Irreversibility of the crack phase field is assured globally using the active-set reduced-space method [57]. A trial point stepper [58] enhances the adaptive load stepping, restricting the increment size close to sudden changes in the dissipated energy.

4.2. The verification and validation of the phase field model for wood

In [51], the phase field model for wood is qualitatively assessed by simulating the fracture of a single-edge notched specimen with tensile loading in the vertical direction, and a board with a single knot and spatially varying principal material orientation. For the single-edge notched specimen, the fiber orientation increases from parallel to the load direction to align with the load direction. Figure 9 shows that as the fiber angle increases, the crack continues to follow the weak interface along the material structure until an energy state at the diffuse crack tip leads to a dominant energy release for a crack perpendicular to the fiber. This results in the often observed zig-zag pattern of cracks in wood [36]. Eventually, the crack transitions from a radial crack to a purely longitudinal one.

Figure 9. The transition of failure modes with increasing fiber orientation. (a) shows only cracks following the weak interface along the fiber. (b) shows the interaction of crack perpendicular to the radial and the longitudinal direction (zig-zag pattern); finally, at a certain fiber angle, cracks form exclusively perpendicular to the fiber (c).
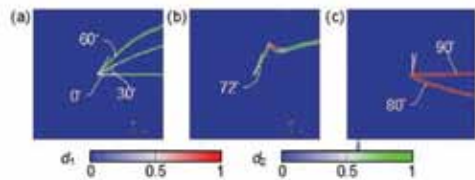
Slika 9. Promjena oblika loma s povećanjem orijentacije vlakna. (a) prikazuje samo pukotine koje prate slabi spoj duž vlakna. (b) prikazuje međudjelovanje pukotine okomito na radijalni i uzdužni smjer (cik-cak uzorak) i konačno, za određeni kut vlakna, pukotine nastaju isključivo okomito na vlakno (c).

The single-edge notched specimen demonstrates that the model can reproduce common crack patterns found in wood. Figure 10 displays the fully cracked state of the specimen with a single knot. As anticipated, the crack follows the fiber orientation until it encounters the knot. At the knot, it propagates along the weak interface between the clear wood and knot material. This example underscores that the influence of the wood's microstructure on macroscopic cracks can be captured using a multi-phase field model and the structural tensor.

Figure 10. The fully cracked state of the single knot specimen. From the initial notch, the crack keeps following the fiber direction until it reaches the knot. At the knot (dark gray), it travels along the interface zone.
Slika 10. Potpuno puknuto stanje uzorka s jednim čvorom. Od početnog zareza, pukotina prati smjer vlakana sve dok ne dođe do čvora. Kod čvora (tamnosivo), putuje duž zone spoja.
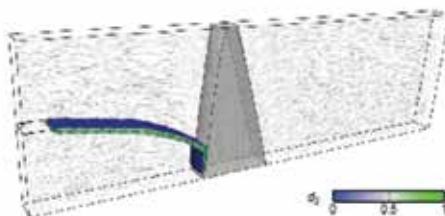
The qualitative assessment confirms that the phase field model for wood is capable of accounting for effects arising from the wood's microstructure. In [52], the model was validated using experimental data from literature. Three different setups were considered: A single edge notched beam (SENB) [59, 37], a double cantilever beam (DCB) [60], and an end-notched beam (ENB) [61]. Figure 11 shows that the response graph for the SENB and the DCB tests aligns very well with the experimental data. In both cases, the tensile strength and fracture energy release rate needed to reproduce the experimental results are within the known range for wood. For the SENB test, it was possible to capture the significantly smaller reaction force for cracks forming in the TL-plane than cracks in the RL-plane using the same initial configuration of the phase field model.
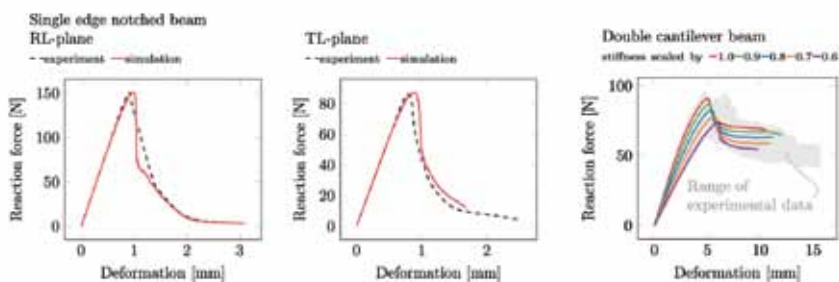
Figure 11. Response graphs for two differently configured SENB tests (crack in RL-plane or TL-plane) and the DCB test. The range of the experimental data is very well captured in all simulations.
Slika 11. Grafički prikazi odziva za dva različito konfigurirana SENB testa (pukotina u RL-ravnini ili TL-ravnini) i DCB test. Područje eksperimentalnih podataka vrlo je dobro obuhvaćeno u svim simulacijama.

The SENB and the DCB tests are both standardized tests for mode-I fracture, where the direction of the load aligns with the normal vector of the crack. Consequently, the effects of the material structure are minimal in these tests. In contrast, the ENB test is a mode-II test, where the structural tensor and the multi-phase field model significantly influence the outcome. Figure 12 illustrates that the structural tensor enables the replication of the horizontal crack observed in the experiments. Additionally, the simulation response falls within the range of the experimentally obtained results.

To ensure that the material parameters tuned on a single model are not model-specific, the tensile strength and fracture energy release rate from the SENB test in [59] are reused for the ENB test. Once again, the result is within the range of the experimental data. This underscores that the phase field model for wood functions as a material model applicable to different test setups, and is not merely a tuned approximation of a specific test specimen.
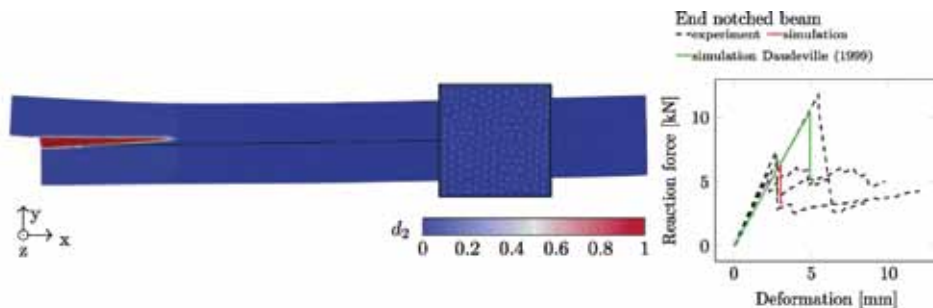
Figure 12. Cracked specimen and response graph for the ENB test. The crack is horizontal, matching the experimental observations, and the model's response is within the experimental range.
Slika 12. Raspuknuti uzorak i grafički prikaz odziva za ENB test. Pukotina je vodoravna, odgovara eksperimentalnim zapažanjima, a odziv modela je unutar područja eksperimenta.

In conclusion, the phase field model for orthotropic non-brittle materials with preferential fracture planes and multiple failure mechanisms [51, 52] has shown its capability to reproduce common crack patterns found in wood, and to match the experimental results of various wood tests closely. The model's general applicability is ensured by its flexible solver design and its reliance on physically interpretable, specimen-independent input parameters such as tensile strength and fracture energy release rate.

However, one of the challenges that remain with this model is the requirement of a small mesh size for proper crack modeling. This requirement can lead to excessive computation time. Therefore, further research is needed in the area of possible model simplification or the application of adaptive mesh refinement strategies.

Despite this challenge, the model provides a valuable tool for understanding and predicting the complex behavior of wood under different loading conditions. Due to the fundamental assumptions of the phase field theory of fracture, the model can handle examples with complex 3D crack topologies. This makes it possible to tackle longstanding problems in timber engineering, such as the simulation of fracture mechanics in wooden boards with multiple knots. Such simulations are crucial for understanding and predicting the behavior of wooden structures under real-world conditions, leading to safer and more efficient designs.

5. SUMMARY AND CONCLUDING REMARKS

Chapter 1 introduces the topic broadly and delineates the challenges and prospects of numerical modeling in timber engineering.

Chapter 2 presents a model for moisture transport both below and above the fiber saturation point. This model is validated with a consistent set of input variables across seven independent tests or simulation results drawn from literature. The overall agreement is very good, demonstrating that it is entirely feasible to depict different drying or infiltration scenarios in wood using a uniform simulation tool. Further improvements in the predictive accuracy of such models will necessitate more well-documented identification and validation experiments.

The potential of such models is exemplified in Section 2.4. The wood moisture content of a cross-laminated timber cross-section is depicted under a realistic ambient climate of 14 months. In contrast to experimental investigations, simulations permit the moisture content to be ascertained at any point in the cross-section and at any moment of loading. The wealth of information gathered in this manner is substantial and can be utilized, for instance, in the development of engineering estimation formulas, as demonstrated in Section 2.4.

In Chapter 3, we present a simulation concept for predicting the bending strength of glued laminated timber. Our validation, based on 40 bending tests, demonstrates a satisfactory agreement with our predictions. To predict the so-called size effect, we executed a simulation program encompassing 8840 GLT beams, ranging from 165 mm to 3300 mm in depth. We utilized advanced modeling concepts, including discrete cracking and plasticity. Our observations revealed a decreasing characteristic bending strength with increasing beam height, and an almost constant mean modulus of elasticity across both strength classes. In conclusion, the effective material behavior of the GLT is influenced by its dimensions. This influence is challenging to capture experimentally for larger

beams; however, numerical simulations appear to be a promising avenue for achieving this understanding.

In order to enhance the computational depiction of wooden components further, significant attention must be devoted to modeling the quasi-brittle failure mechanisms inherent in wood. An especially promising approach is the phase field method, as proposed in Chapter 4. However, the original formulation of the phase field method is limited to isotropic materials, and does not account for preferential fracture planes defined by the wood's microstructure. In this work, we extend the method to accommodate orthotropic constitutive behavior and preferred directions of crack propagation. We demonstrate that by utilizing a stress-based split and multiple phase field variables with preferential fracture planes, combined with a hybrid phase field approach, a comprehensive framework can be established for simulating anisotropic, inhomogeneous materials, such as wood.

This is crucial, as the growing variety of wood products, fastener systems, and the escalating complexity of timber engineering structures, as mentioned in the introduction, can only be feasibly managed in the future through a smart integration of physical experiments and computational simulation concepts. Here, manageable means that the mechanical performance of all chosen design details can be predicted accurately enough to ensure efficient, economical, and reliable execution. The goal ought to be further enhancement of the competitiveness of wood compared to other building materials, and ensuring the ongoing advancement of timber engineering.

Acknowledgement

LITERATURE

1. J. Siau (1984) *Transport Processes in Wood.* Berlin Heidelberg New York Tokyo: Springer-Verlag.
2. M. Autengruber, M. Lukacevic, J. Füssl (2020) *Finite-element-based moisture transport model for wood including free water above the fiber saturation point.* International Journal of Heat and Mass Transfer 161, 120228.
3. C. Skaar (1988) *Wood-Water Relations.* Berlin Heidelberg: Springer-Verlag.
4. K. Krabbenhøft, L. Damkilde (2004) *Double porosity models for the description of water infiltration in wood.* Wood Science and Technology 38, p. 641–659.
5. H.D. Tiemann (1906) *Effect of moisture upon the strength and stiffness of wood.* US Department of Agriculture, Forest Service.

6. E.T. Engelund, L.G. Thygesen, S. Svensson, C.A.S. Hill (2012) *A critical discussion of the physics of wood-water interactions.* Wood Science and Technology 47, p. 141–161. 2012.

7. ÖNORM EN B 1995-1-1:2019-06-01 (2019)*, Eurocode 5: Bemessung und Konstruktion von Holzbauten - Teil 1-1: Allgemeines - Allgemeine Regeln und Regeln für den Hochbau - Konsolidierte Version mit nationalen Festlegungen, nationalen Erläuterungen und nationalen Ergänzungen zur Umsetzung der ÖNORM EN 1995-1-1.* Wien: Austrian Standards International, June 2019.

8. S. Svensson, G. Turk, T. Hozjan (2011) *Predicting moisture state of timber members in a continuously varying climate.* Engineering Structures 33, p. 3064–3070.

9. D. Konopka, M. Kaliske (2018) *Transient multi-Fickian hygro-mechanical analysis of wood.* Computers & Structures 197, p. 12–27.

10. H. L. Frandsen, L. Damkilde, S. Svensson (2007) *A revised multi-Fickian moisture transport model to describe non-Fickian effects in wood.* Holzforschung 61, p. 563–572.

11. K. Krabbenhøft, L. Damkilde (2004) *A model for non-Fickian moisture transfer in wood.* Materials and Structures 37, p. 615–622.

12. S.V. Dvinskikh, M. Henriksson, A.L. Mendicino, S. Fortino, T. Toratti (2011) *NMR imaging study and multi-Fickian numerical simulation of moisture transfer in Norway spruce samples.* Engineering Structures 33, p. 3079–3086.

13. J. Eitelberger, K. Hofstetter, S. V. Dvinskikh (2011) *A multi-scale approach for simulation of transient moisture transport processes in wood below the fiber saturation point.* Composites Science and Technology 71, p. 1727–1738.

14. P. Perré (2015) *The proper use of mass diffusion equations in drying modeling: Introducing the drying intensity number.* Drying Technology 33, p. 1949–1962.

15. J. Eriksson, H. Johansson, J. Danvind (2007) *A mass transport model for drying wood under isothermal conditions.* Drying Technology 25, p. 433–439.

16. S. Sandoval-Torres, A. Pérez-Santiago, E. Hernández-Bautista, (2019) *Drying model for softwood and moisture patterns measured by magnetic resonance imaging.* Drying Technology 37, p. 458–467.

17. Ö. Gezici-Koç, S.J.F. Erich, H.P. Huinink, L.G.J. van der Ven, O.C.G. Adan (2017) *Bound and free water distribution in wood during water uptake and drying as measured by 1D magnetic resonance imaging.* Cellulose 24, p. 535–553.

18. P. Perré, I.W. Turner (1999) *A 3-D version of TransPore: a comprehensive heat and mass transfer computational model for simulating the drying of porous media.* International Journal of Heat and Mass Transfer 42, p. 4501–4521.

19. M. Autengruber, M. Lukacevic, C. Gröstlinger, J. Füssl, J. Eberhardsteiner (2021) *Numerical assessment of wood moisture content-based assignment to service classes in EC 5 and prediction concept for moisture-induced stresses solely using relative humidity data.* Engineering Structures 245, 112849.

20. M. Autengruber, M. Lukacevic, C. Gröstlinger, J. Füssl (2021) *Finite-element-based prediction of moisture-induced crack patterns for cross sections of solid wood and glued laminated timber exposed to a realistic climate condition.* Construction and Building Materials 271, 121775.

21. M. Autengruber, M. Lukacevic, G. Wenighofer, R. Mauritz, J. Füssl (2021) *Finite-element-based concept to predict stiffness, strength, and failure of wood composite I-joist beams under various loads and climatic conditions.* Engineering Structures 245, 112908.

22. M. Lukacevic, M. Autengruber, T. Raimer, J. Eberhardsteiner, J. Füssl (2021) *Effect of cast-in-place concrete application on moisture distribution in timber-concrete composite floors with notched connections, investigated via finite element simulations.* Journal of Building Engineering 42, 103005.

23. DIN EN 14080 (2013) Holzbauwerke – Brettschichtholz und Balkenschichtholz – Anforderungen.

24. DIN EN 408 (2010) Holzbauwerke – Bauholz für tragende Zwecke und Brettschichtholz – Bestimmung einiger physikalischer und mechanischer Eigenschaften.

25. G. Kandler, M. Lukacevic, J. Füssl (2018) *Experimental study on glued laminated timber beams with well-known knot morphology.* European Journal of Wood and Wood Products 76, p. 1435–1452.

26. W. Weibull (1939) *A statistical theory of strength of materials. IVB-Handl.*

27. L. Blank, G. Fink, R. Jockwer, A. Frangi (2017) *Quasi-brittle fracture and size effect of glued laminated timber beams.* European Journal of Wood and Wood Products, p. 1–15.

28. G. Fink, A. Frangi, J. Kohler (2015) *Probabilistic approach for modelling the load-bearing capacity of glued laminated timber.* Engineering Structures 100, p. 751–762.

29. C. Vida, M. Lukacevic, J. Eberhardsteiner, J. Füssl (2022) *Modeling approach to estimate the bending strength and failure mechanisms of glued laminated timber beams.* Engineering Structures 255, 113862.

30. K. Hofstetter, C. Hellmich, J. Eberhardsteiner (2007) *Micromechanical modeling of solid-type and plate-type deformation patterns within softwood materials. A review and an improved approach.* Holzforschung 61, p. 343–351.

31. G. Kandler, M. Lukacevic, J. Füssl, C. Zechmeister, S. Wolff (2018) *Stochastic engineering framework for timber structural elements and its application to glued laminated timber beams.* Construction and Building Materials 190, p. 573–592.

32. M. Lukacevic, W. Lederer, J. Füssl (2017) *A microstructure-based multisurface failure criterion for the description of brittle and ductile failure mechanisms of clearwood.* Engineering Fracture Mechanics 176, p. 83–99.

33. M. Lukacevic, J. Füssl, R. Lampert (2015) *Failure mechanisms of clear wood identified at wood cell level by an approach based on the extended finite element method.* Engineering Fracture Mechanics 144, p. 158–175.

34. S. Pech, M. Lukacevic, J. Füssl (2021) *A robust multisurface return-mapping algorithm and its implementation in Abaqus*. Finite Elements in Analysis and Design 190, 103531.

35. M. Frese (2016) *Computergestützte Verfahren zur pragmatischen Beurteilung der Tragwiderstände von Brettschichtholz.* Zusammenfassung exemplarischer Simulationsstudien 31, KIT Scientific Publishing.

36. I. Smith, E. Landis, M. Gong, *Fracture and Fatigue in Wood (2003)* Chichester, West Sussex, England ; Hoboken, NJ: J. Wiley.

37. N. Dourado, S. Morel, M. F. S. F. de Moura, G. Valentin, J. Morais (2008) *Comparison of Fracture Properties of Two Wood Species through Cohesive Crack Simulations.* Composites Part A: Applied Science and Manufacturing 39, p. 415–427.

38. S. Vasic, I. Smith, E. Landis (2002) *Fracture Zone Characterization - Micro-mechanical Study.* Wood and Fiber Science 34, p. 42–56.

39. A. A. Griffith, G. I. Taylor (1921) *VI. The Phenomena of Rupture and Flow in Solids.* Philosophical Transactions of the Royal Society of London. Series A, Containing Papers of a Mathematical or Physical Character 221, p. 163–198.

40. B. Bourdin, G. A. Francfort, J.-J. Marigo (2000) *Numerical Experiments in Revisited Brittle Fracture.* Journal of the Mechanics and Physics of Solids 48, p. 797–826.

41. B. Bourdin, G. A. Francfort, J.-J. Marigo (2008) *The Variational Approach to Fracture.* Springer-Verlag GmbH.

42. G. A. Francfort, J.-J. Marigo (1998) *Revisiting Brittle Fracture as an Energy Minimization Problem.* Journal of the Mechanics and Physics of Solids 46, p. 1319–1342.

43. C. Miehe, F. Welschinger, M. Hofacker (2010) *Thermodynamically Consistent Phase-Field Models of Fracture: Variational Principles and Multi-Field FE Implementations.* International Journal for Numerical Methods in Engineering 83, p. 1273–1311.

44. J. Bleyer, R. Alessi (2018) *Phase-Field Modeling of Anisotropic Brittle Fracture Including Several Damage Mechanisms.* Computer Methods in Applied Mechanics and Engineering 336, p. 213–236.

45. J. D. Clayton, J. Knap (2014) *A Geometrically Nonlinear Phase Field Theory of Brittle Fracture.* International Journal of Fracture 189, p. 139–148.

46. V. Hakim, A. Karma (2005) *Crack Path Prediction in Anisotropic Brittle Materials.* Physical Review Letters 95, 235501.

47. S. Teichtmeister, D. Kienle, F. Aldakheel, M.-A. Keip (2017) *Phase Field Modeling of Fracture in Anisotropic Brittle Solids.* International Journal of Non-Linear Mechanics 97, p. 1–21.

48. J.-Y. Wu, V. P. Nguyen (2018) *A Length Scale Insensitive Phase-Field Damage Model for Brittle Fracture.* Journal of the Mechanics and Physics of Solids 119, p. 20–42.

49. J. Carlsson, P. Isaksson (2020) *Simulating Fracture in a Wood Microstructure Using a High-Resolution Dynamic Phase Field Model.* Engineering Fracture Mechanics 232, 107030.

50. D. Supriatna, B. Yin, D. Konopka, M. Kaliske (2022) *An Anisotropic Phase-Field Approach Accounting for Mixed Fracture Modes in Wood Structures within the Representative Crack Element Framework.* Engineering Fracture Mechanics 269, 108514.

51. S. Pech, M. Lukacevic, J. Füssl (2022) *A Hybrid Multi-Phase Field Model to Describe Cohesive Failure in Orthotropic Materials, Assessed by Modeling Failure Mechanisms in Wood.* Engineering Fracture Mechanics 271, 108591.

52. S. Pech, M. Lukacevic, J. Füssl (2022) *Validation of a Hybrid Multi-Phase Field Model for Fracture of Wood.* Engineering Fracture Mechanics 275, 108819.

53. C. Steinke, M. Kaliske (2018) *A Phase-Field Crack Model Based on Directional Stress Decomposition.* Computational Mechanics, p. 1019—1046.

54. C. Miehe, M. Hofacker, F. Welschinger (2010) *A Phase Field Model for Rate-Independent Crack Propagation: Robust Algorithmic Implementation Based on Operator Splits.* Computer Methods in Applied Mechanics and Engineering 199, p. 2765–2778.

55. M. Ambati, T. Gerasimov, L. D. Lorenzis (2014) *A Review on Phase-Field Models of Brittle Fracture and a New Fast Hybrid Formulation.* Computational Mechanics 55, p. 383–405.

56. T. Hu, J. Guilleminot, J. E. Dolbow (2020) *A Phase-Field Model of Fracture with Frictionless Contact and Random Fracture Properties: Application to Thin-Film Fracture and Soil Desiccation.* Computer Methods in Applied Mechanics and Engineering 368, 113106.

57. H. Yang, C. Yang, S. Sun (2016) *Active-Set Reduced-Space Methods with Nonlinear Elimination for Two-Phase Flow Problems in Porous Media.* SIAM Journal on Scientific Computing 38, p. B593–B618.

58. A. Gupta, U. M. Krishnan, R. Chowdhury, A. Chakrabarti (2020) *An Auto-Adaptive Sub-Stepping Algorithm for Phase-Field Modeling of Brittle Fracture.* Theoretical and Applied Fracture Mechanics 108, 102622.

59. L. Daudeville (1999) *Fracture in Spruce: Experiment and Numerical Analysis by Linear and Non Linear Fracture Mechanics.* Holz als Roh-und Werkstoff 57, p. 425–432.

60. M. F. S. F. de Moura, J. J. L. Morais, N. Dourado (2008) *A New Data Reduction Scheme for Mode I Wood Fracture Characterization Using the Double Cantilever Beam Test.* Engineering Fracture Mechanics 75, p. 3852–3865.

61. K. Rautenstrauch, B. Franke, S. Franke, K. U. Schober (2008) *A New Design Approach for End-Notched Beams: View in Code.* in Paper No. CIB-W18/41-6-2, Proc.

NUMERIČKO MODELIRANJE U DRVNOM INŽENJERSTVU – PRIJENOS VLAGE I KVAZI-KRTI LOM

Sažetak

S rastućom popularnosti drvenih konstrukcija i povećanjem složenosti drvenih inženjerskih

struktura, alati za njihovu numeričku simulaciju sve više dobivaju na važnosti. Procesi prijenosa vlage i ponašanje pri kvazi-krtom lomu, koje je teško opisati, posebno predstavljaju velike izazove i teme od velike važnosti za konstrukcijsku praksu. Iz toga razloga, ovaj članak prikazuje koncepciju numeričkog modeliranja predviđanja gradijenata vlage, procjene efektivne krutosti i čvrstoće, te numeričko određivanje mogućih mehanizama loma u drvenim konstrukcijskim komponentama. Prikazani postupci su validirani korištenjem eksperimentalnih testnih programa te su razmatrani pritom nastali izazovi. Odabrani rezultati u konačnici pokazuju mogućnosti primjene, a isto tako i važnost tih metoda u drvnom inženjerstvu.

Ključne riječi: drvo; modeliranje prijenosa vlage; kvazi-krti lom; GLT; postupak faznog polja.

Josef Eberhardsteiner
Vienna University of Technology
Institute for Mechanics of Materials and Structures
Karlsplatz 13/202, A-1040 Wien, Austria
E-mail: josef.eberhardsteiner@tuwien.ac.at

Maximilian Autengruber
Vienna University of Technology
Institute for Mechanics of Materials and Structures
Karlsplatz 13/202, A-1040 Wien, Austria
E-mail: maximilian.autengruber @tuwien.ac.at

Markus Lukacevic
Vienna University of Technology
Institute for Mechanics of Materials and Structures
Karlsplatz 13/202, A-1040 Wien, Austria
E-mail: markus.lukacevic @tuwien.ac.at

Josef Füssl
Vienna University of Technology
Institute for Mechanics of Materials and Structures
Karlsplatz 13/202, A-1040 Wien, Austria
E-mail: josef.fuessl@tuwien.ac.at

Sebastian Pech
Vienna University of Technology
Institute for Mechanics of Materials and Structures
Karlsplatz 13/202, A-1040 Wien, Austria
E-mail: sebastian.pech@tuwien.ac.at

Christoffer Vida
Vienna University of Technology
Institute for Mechanics of Materials and Structures
Karlsplatz 13/202, A-1040 Wien, Austria
E-mail: christoffer.vida@tuwien.ac.at

Markus Königsberger
Vienna University of Technology
Institute for Mechanics of Materials and Structures
Karlsplatz 13/202, A-1040 Wien, Austria
E-mail: markus.koenigsberger @tuwien.ac.at